Gyrokinetic particle simulation of microturbulence for general magnetic geometry and experimental profiles

Yong Xiao,[1,2,a)] Ihor Holod,[2] Zhixuan Wang,[2] Zhihong Lin,[2,3] and Taige Zhang[1]
[1]*Institute for Fusion Theory and Simulation, Zhejiang University, Hangzhou 310027, China*
[2]*Department of Physics and Astronomy, University of California, Irvine, California 92697, USA*
[3]*Fusion Simulation Center, Peking University, Beijing 100871, China*

(Received 25 August 2014; accepted 30 January 2015; published online 25 February 2015)

Developments in gyrokinetic particle simulation enable the gyrokinetic toroidal code (GTC) to simulate turbulent transport in tokamaks with realistic equilibrium profiles and plasma geometry, which is a critical step in the code–experiment validation process. These new developments include numerical equilibrium representation using B-splines, a new Poisson solver based on finite difference using field-aligned mesh and magnetic flux coordinates, a new zonal flow solver for general geometry, and improvements on the conventional four-point gyroaverage with nonuniform background marker loading. The gyrokinetic Poisson equation is solved in the perpendicular plane instead of the poloidal plane. Exploiting these new features, GTC is able to simulate a typical DIII-D discharge with experimental magnetic geometry and profiles. The simulated turbulent heat diffusivity and its radial profile show good agreement with other gyrokinetic codes. The newly developed nonuniform loading method provides a modified radial transport profile to that of the conventional uniform loading method. © *2015 AIP Publishing LLC*.
[http://dx.doi.org/10.1063/1.4908275]

I. INTRODUCTION

A complete understanding of the physics of anomalous transport is critical for the design of future magnetic fusion reactors.[1] It is generally believed that turbulence at the ion gyroradius scale (micro-scale) leads to the anomalous transport[2] observed in experiments. For low-β (defined as the ratio of kinetic pressure to magnetic pressure) and high-temperature toroidal plasmas, electrostatic modes might provide the greatest contribution to turbulent transport. The ion temperature gradient (ITG) mode[2,3] and collisionless trapped electron mode[4] are two prominent candidates in accounting for ion and electron turbulent transport, respectively. After several decades' development, massively parallel gyrokinetic simulation based on first-principles has emerged as a major tool in the investigation of the complex physics of turbulent transport.[5]

There are several stages to the code development for these large-scale gyrokinetic simulations. First, the code is implemented based on the gyrokinetic model and then verified by some analytical theory and other numerical codes to ensure that the code faithfully represents the simulation model.[6,7] The next step is to use the existing code to study interesting but complex physics, such as the saturation and transport mechanisms of turbulence.[8,9] The third step is called code validation,[10–12] which is usually performed in parallel to the second stage. In this step, the gyrokinetic simulation is performed using realistic experimental parameters. The simulation results, such as the transport flux, and temporal and spatial characteristics of the turbulence, are compared with the experimental measurements not only to help explain the experimental observations, but also to verify whether the simulation model has captured the essential physics of the turbulent transport. Following the comprehensive comparisons between codes, simulation models, and experiments, the code is expected to have predictive power. The ultimate goal of gyrokinetic code development is to guide new campaigns of experiments and to help design the next generation of fusion devices.

Current efforts on gyrokinetic code development still focus on the first three stages and in particular, the code validation step is considered critical in this roadmap. The main purpose of this article is to report the recent progress of the global gyrokinetic toroidal code (GTC)[5,13] in incorporating general equilibrium magnetic geometry and real experimental profiles to simulate turbulent transport in tokamak experiments. In fact, these new features reported in this work have already been used successfully to validate GTC simulations of Alfven eigenmodes[14–16] in DIII-D experiments and to study the trapped electron mode instability in the pedestal of DIII-D H-mode plasmas.[17] The general geometry capability can also be readily used in conjunction with recent upgrades of GTC physics models for global simulations of macroscopic MHD instabilities excited by equilibrium current[18] and radio frequency waves in tokamaks.[19]

In this work, we develop a numerical scheme based on B-splines to calculate the equilibrium quantities on the computational grids and to evaluate the field quantities at the particle's position. This new feature enables the use of the numerical magnetic equilibrium produced by MHD equilibrium codes such as EFIT,[20,21] VMEC,[22] and the transport code TRANSP.[22,23] To accommodate the general magnetic geometry, we improve the conventional four-point average method[24] to calculate the gyroaverage, and implement a new

[a)]Electronic mail: yxiao@zju.edu.cn. Tel.: (86)57187952649

gyrokinetic Poisson solver based on the Pade approximation. As field-aligned magnetic coordinates are employed, we can solve the gyrokinetic Poisson equation in the perpendicular plane rather than the poloidal plane. This new Poisson solver in the GTC code is able to simulate small-aspect-ratio tokamaks such as the NSTX in addition to the conventional large-aspect-ratio tokamaks. A new zonal flow solver is developed for the general magnetic geometry. We also implement a nonuniform loading method for the background marker distribution in addition to the conventional uniform loading method.

We use DIII-D discharge #101391 as a benchmark case for these new developments in the GTC. In the simulation, we include kinetic electrons and find that this discharge is dominated by ITG instabilities. We compare the heat diffusivity for different gyrokinetic Poisson solvers and different marker loading methods. The new gyrokinetic Poisson solver provides about the same level of turbulent transport as the conventional four-point average method. In addition, the nonuniform loading method provides about the same volume-averaged turbulent transport as the conventional uniform loading. However, the radial profile of the turbulent transport is different for these two loading methods, which is attributed to the stabilizing effect of the gyroaverage, i.e., the finite Larmor radius (FLR) effect. The simulation results are compared with those from GYRO[25,26] and good agreement is obtained.

The remainder of this paper is organized as follows. In Sec. II, we introduce the numerical representation of equilibrium plasma quantities, especially the B-spline interpolation. In Sec. III, the perturbative δf method used to solve the gyrokinetic equation and the particle-pushing scheme in general magnetic geometry are reviewed for completeness. We then explain how to use the Pade approximation to solve the gyrokinetic Poisson equation and the associated zonal flow component in Sec. III, where the conventional four-point average method is also improved. The finite difference scheme is used to discretize the Laplacian operator, and it is verified in Sec. IV. In Sec. V, based on these improvements, a gyrokinetic turbulence simulation by GTC is benchmarked with other code using the DIII-D experimental parameters. A summary and discussion are provided in Sec. VI.

II. NUMERICAL REPRESENTATION OF EQUILIBRIUM PLASMA QUANTITIES

In plasma turbulence studies, we often divide the physical quantities into an equilibrium part and a fluctuating part. The equilibrium quantities obey the MHD equilibrium, i.e., the Grad–Shafranov equation, while the fluctuating part is driven by various instabilities that lead to turbulent transport. The equilibrium magnetic configurations used by the gyrokinetic simulation are either from analytic models such as the simple circular cross section or Miller equilibrium, or from other numeric equilibrium codes such as EFIT[20,21] or VMEC.[22] The equilibrium in tokamaks can be described better by magnetic flux coordinates rather than Cartesian coordinates, because most important equilibrium quantities, such as plasma temperature and density, can be shown to depend on the magnetic flux only. The GTC employs magnetic flux coordinates (ψ, θ, ζ) to represent the electromagnetic fields and plasma profiles, where ψ is the poloidal magnetic flux, θ is the poloidal angle, and ζ is the toroidal angle. The equilibrium magnetic field can be represented either in the following covariant form:

$$\mathbf{B}_0 = g\nabla\zeta + I\nabla\theta + \delta\nabla\psi, \tag{1}$$

or in the contravariant form

$$\mathbf{B}_0 = q\nabla\psi \times \nabla\theta + \nabla\zeta \times \nabla\psi. \tag{2}$$

Then, the transformation Jacobian takes the following form:

$$J^{-1} \equiv \nabla\psi \times \nabla\theta \cdot \nabla\zeta = \frac{{B_0}^2}{gq + I}. \tag{3}$$

If the Jacobian is chosen properly such that (ψ, θ, ζ) are the Boozer coordinates, the toroidal current $2\pi g$ and poloidal current $2\pi I$ can be represented by a sole function of ψ, i.e., $g = g(\psi), I = I(\psi)$.

The GTC code inputs the numerical magnetic equilibrium and plasma profiles from EFIT/VMEC by transforming the equilibrium quantities defined in the toroidal coordinates (R, Z, ϕ) to those defined in the magnetic coordinates (ψ, θ, ζ). However, the EFIT outputs only provide equilibrium quantities on a coarse mesh, which usually contains a few tens of grid points in the radial or poloidal direction, as shown in Fig. 1. This equilibrium mesh cannot be used to simulate micro-scale turbulence on the order of the ion gyroradius (ρ_i), which requires a much denser mesh of grid points, e.g., hundreds to thousands of grid points in the radial

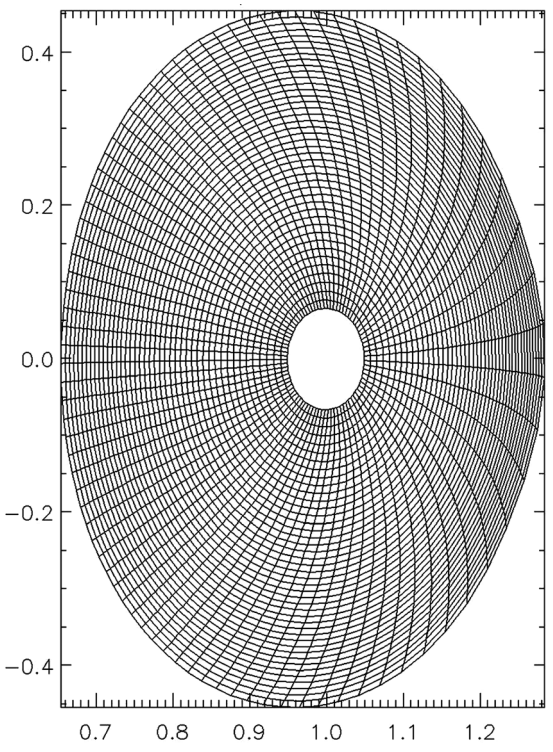

FIG. 1. Equilibrium mesh from EFIT data. The solid lines are drawn along constant ψ and θ.

and poloidal directions for the size of a realistic tokamak, as sketched by the unstructured computational grids in Fig. 2. Therefore, it is necessary to map the coarse experimental mesh to the fine computational mesh to achieve sufficient numerical accuracy. In the GTC code first-order continuous B-splines are currently implemented for the 1D and 2D functions to interpolate the complicated magnetic geometry and plasma profiles which provide a good compromise between high numerical confidence and reasonable computation efficiency. Generally, two classes of function are involved in describing the magnetic geometry and plasma profiles in axisymmetric systems such as tokamaks: a 1D function $f(\psi)$ to describe quantities such as the temperature profile $T(\psi)$, and a 2D function $f(\psi,\theta)$ to describe quantities such as the equilibrium magnetic field $B(\psi,\theta)$. The detailed implementations of these functions are illustrated in Appendix A.

III. GYROKINETIC EQUATION AND POISSON SOLVER IN GENERAL MAGNETIC GEOMETRY

The gyrokinetic particle simulation uses the particle-in-cell method to solve the gyrokinetic equation, which is essentially a Monte-Carlo approach to solve the reduced dynamic equation in the 5D phase space of $(\psi,\zeta,\theta,v_\parallel,\mu)$, where $\mu = mv_\perp{}^2/2B$ is the magnetic moment and $v_\parallel$ is the parallel velocity for the particle. In the GTC turbulence simulation, we apply gyrokinetics for the ion and drift kinetics for the electron, because our focus is on the turbulence on the ion gyroradius scale. The ion distribution function $f_i \approx f_{Mi} + \delta f_i$ with the perturbed guiding center distribution function δf_i satisfies the following gyrokinetic equation:[27]

$$\frac{d\delta f_i}{dt} \equiv \left[\frac{\partial}{\partial t} + \left(v_\parallel \mathbf{b} + \mathbf{v}_d + \langle \mathbf{v}_E\rangle_\varphi\right)\cdot\nabla - \mathbf{b}^*\cdot\nabla\left(\mu B + Z_i e\langle\phi\rangle_\varphi\right)\frac{\partial}{m_i\partial v_\parallel}\right]\delta f_i = -f_{Mi}\left(\langle \mathbf{v}_E\rangle_\varphi\cdot\nabla \ln f_{Mi} - \mathbf{b}^*\cdot\nabla\langle\phi\rangle_\varphi\frac{Z_i e\partial}{m_i\partial v_\parallel}\ln f_{Mi}\right). \quad (4)$$

In this equation, $\mathbf{b}^* = \mathbf{b} + \frac{m_i c}{Z_i eB} v_\parallel \nabla\times\mathbf{b}$, $\mu = \frac{m_i v_\perp{}^2}{2B}$, $\langle \mathbf{v}_E\rangle_\varphi = \frac{c\mathbf{b}\times\nabla\langle\phi\rangle_\varphi}{B}$ with $\langle\phi\rangle_\varphi = \frac{1}{2\pi}\int\phi(\mathbf{x})\delta(\mathbf{x}-\mathbf{R}-\boldsymbol{\rho})d\mathbf{x}d\varphi$ as the gyroaveraged electrostatic potential, and $\mathbf{v}_d = \mathbf{v}_c + \mathbf{v}_g$ with $\mathbf{v}_c = \frac{v_\parallel{}^2}{\Omega_i}\nabla\times\mathbf{b}$ and $\mathbf{v}_g = \frac{\mu}{m_i\Omega_i}\mathbf{b}\times\nabla B$. We decompose the electrostatic potential to a flux-surface averaged component (zonal component) and a fluctuating component, i.e., $\phi = \langle\phi\rangle + \delta\phi$ with $\langle\delta\phi\rangle = 0$. The electrons might respond mostly to the fluctuating potential adiabatically because of their fast motion. Therefore, it is convenient to write the electron distribution function as $f_e \approx f_{Me} + \frac{e\delta\phi}{T_e}f_{Me} + \delta g_e$ with $\frac{e\delta\phi}{T_e} \ll 1$ and δg_e to satisfy the following drift kinetic equation:[28]

$$\left[\frac{\partial}{\partial t} + \left(v_\parallel\mathbf{b} + \mathbf{v}_d + \mathbf{v}_E\right)\cdot\nabla - \mathbf{b}^*\cdot\nabla(\mu B - e\phi)\frac{\partial}{m_e\partial v_\parallel}\right]\delta g_e = -f_{Me}\exp\left(\frac{e\delta\phi}{T_e}\right)\left(\frac{\partial}{\partial t}\left(\frac{e\delta\phi}{T_e}\right) + \delta\mathbf{v}_E\cdot\nabla\ln f_{Me} - (\mathbf{v}_d + \delta\mathbf{v}_E)\cdot\nabla\left(\frac{e\langle\phi\rangle}{T_e}\right)\right), \quad (5)$$

where $\delta\mathbf{v}_E = \frac{c\mathbf{b}\times\nabla\langle\delta\phi\rangle_\varphi}{B}$.

In the δf algorithm, to minimize the Monte-Carlo noise caused by the particle method, the particle weight $w = \delta f/f$ is introduced as an additional attribute to the particles. The evolution of the particle weight is determined by the following equation:[29]

$$\frac{dw}{dt} = \frac{1-w}{F_M}\frac{d\delta f}{dt}. \quad (6)$$

The guiding centers follow equations of motion in the general magnetic geometry for tokamaks, which is discussed in Appendix B.

To close the preceding gyrokinetic equations, we need to solve the following gyrokinetic Poisson equation:

$$\frac{Z_i{}^2 e n_{0i}}{T_i}\left(\phi - \tilde{\phi}\right) = z_i\bar{n}_{i1} - n_{e1}, \quad (7)$$

with $\tilde{\phi} = \frac{1}{2\pi}\int\langle\phi\rangle_\varphi(R)\delta(\mathbf{x}-\mathbf{R}-\rho)F_{Mi}(\mathrm{R},\mu,v_\parallel)d\mathbf{R}d^3v$.[30] For perturbed electron density, it is convenient to write $n_{e1} = (1-\delta_m)n_{e0}e\phi/T_e + \delta n_e{}^{(1)}$ with $\delta_m = 0$ for the electrostatic case and $\delta_m = 1$ for the electromagnetic case. Therefore, we obtain the following gyrokinetic Poisson equation:[13,28,31]

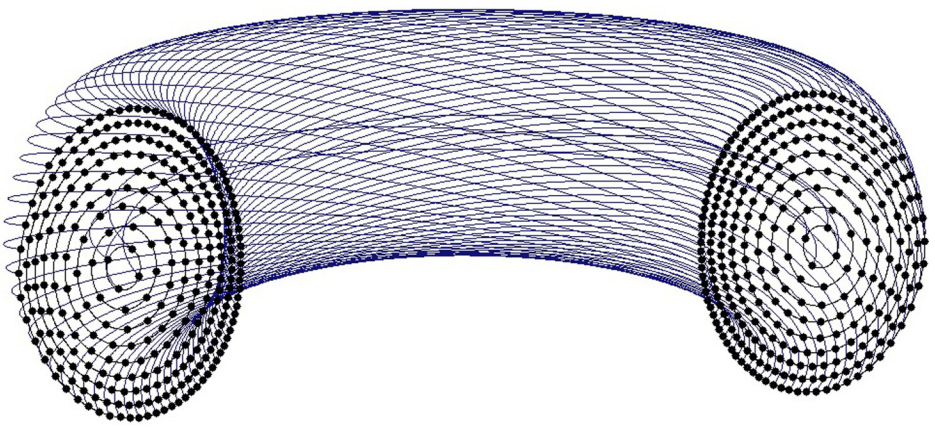

FIG. 2. Unstructured mesh in GTC. Sketch of unstructured field-aligned mesh in GTC. The grids are usually set to make the radial and poloidal grid sizes equal.

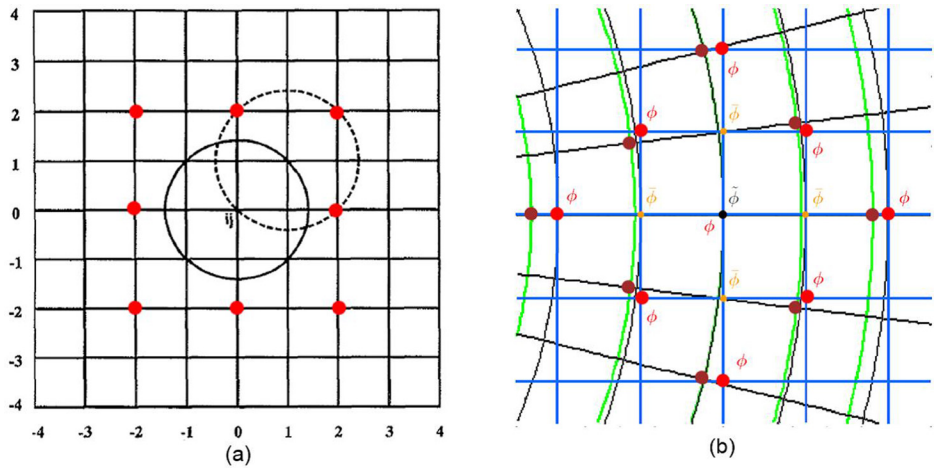

FIG. 3. Four-point average revisited. (a) Eight extra points are required to compute $\tilde{\phi}$ based on the four-point gyroaverage method. (b) The points used to compute $\tilde{\phi}$ in the current GTC (bright red points) capture the global effect, while the points used conventionally (dark red points) are based on the local approximation.

$$\left(\frac{z_i^2 e n_{i0}}{T_i}+\frac{e n_{e0}}{T_e}\delta m\right)\phi-\frac{Z_i^2 e n_{i0}}{T_i}\tilde{\phi}=Z_i\bar{n}_{i1}-\delta n_e{}^{(1)}, \quad (8)$$

with $\overline{n_{i1}}=\int\delta(\mathbf{X}-\mathbf{R}-\rho)\delta f_i d\mathbf{R}d^3v$ and $\delta n_e{}^{(1)}=\int\delta(\mathbf{X}-\mathbf{R}-\rho)\delta g_e d\mathbf{R}d^3v$. There are two approaches to evaluate $\tilde{\phi}$: the four-point average or Pade approximation. The four-point average method is illustrated in Ref. 32, as is shown schematically in Fig. 3(a). However, the four-point method that is conventionally implemented in GTC is only accurate when $r\gg\rho_i$, since it only retains the leading order term in the ρ_i/r expansion and it becomes inaccurate when $r\sim\rho_i$. When approaching the magnetic axis, the flux surface becomes circular and the polar coordinates (r,θ) can be used to illustrate the improved four-point average method. Considering a particular point (r,θ), the four points for the gyroaverage in the conventional four-point average method are $(r+\rho_i,\theta)$, $(r-\rho_i,\theta)$, $(r,\theta+\rho_i/r)$, and $(r,\theta-\rho_i/r)$, as is shown by the dark red points in Fig. 3(b). To capture the global effects, we need to retain higher-order terms, e.g., the second-order correction. As shown by the bright red points in Fig. 3(b), the following four points $(r+\rho_i,\theta)$, $(r-\rho_i,\theta)$, $(r+\rho_i{}^2/r,\theta+\rho_i/r)$, and $(r+\rho_i{}^2/r,\theta-\rho_i/r)$ are chosen for the gyroaverage in the improved four-point average method. It becomes transparent that the change in the radial location for this new average method is of the order of $\rho_i{}^2/r^2$. For the boundary conditions in the gyrokinetic Poisson equation, it is usually set as $\phi(\psi=\psi_0)=\phi(\psi=\psi_1)=0$ because we do not want boundary effects to affect the turbulent transport in the central part of the simulation domain.

We note that in the long wavelength limit $\phi-\tilde{\phi}\approx-\rho_i{}^2\nabla_\perp{}^2\phi$. Hence, one crucial step in verifying the improved four-point average method for the gyrokinetic Poisson equation is to show that it can be used to solve the Poisson problem $-\nabla_\perp{}^2\phi=\delta n$. In the high q limit, the toroidal effects can be ignored. Considering a tokamak with a circular cross section, the Laplacian operator can be approximated as $\nabla_\perp{}^2=\frac{1}{r}\frac{\partial}{\partial r}r\frac{\partial}{\partial r}+\frac{1}{r^2}\frac{\partial^2}{\partial\theta^2}$. This Poisson problem essentially becomes a Bessel problem. Then, if we let $\delta n(r,\theta)=J_m(k_0r)-\frac{J_m(k_0a_1)}{Y_m(k_0a_1)}Y_m(k_0r)$ with $m=6$ and k_0 satisfying $J_m(k_0a_0)Y_m(k_0a_1)-J_m(k_0a_1)Y_m(k_0a_0)=0$, the Poisson equation has an analytic solution $\phi=J_m(k_0r)-\frac{J_m(k_0a_1)}{Y_m(k_0a_1)}Y_m(k_0r)$ under the boundary condition $\phi(r=a_0)=\phi(r=a_1)=0$. As shown in Fig. 4, the solid lines show the analytic solution, while the lines with different shapes show the different numbers of radial grids applied in the numeric calculation. Fig. 4(a) shows the solutions from the conventional local approximation for the four-point average method for different numbers of radial grids, while Fig. 4(b) shows the solution by adding higher-order global corrections to the four-point average method. As can be seen from these figures, the new implementation of the global correction makes the numeric solution closer to the analytic value.

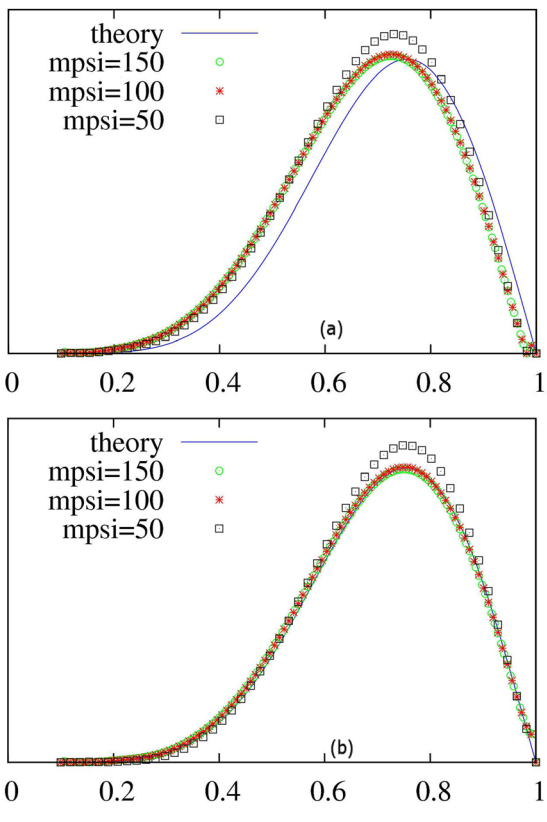

FIG. 4. Verification of four-point average. The four-point averages applied to compute the $\tilde{\phi}$ are verified in the Bessel problem for the following two cases: (a) with local approximation and (b) with global correction.

Next, we discuss the second method to evaluate $\tilde{\phi}$, the Pade approximation, as demonstrated in the following:

$$\tilde{\phi} = \frac{1}{1-\rho_i{}^2\nabla_\perp{}^2}\phi. \tag{9}$$

We decompose the electrostatic potential and density perturbation to a flux-surface averaged component (zonal component) and a fluctuating component, i.e., $\phi = \langle\phi\rangle + \delta\phi$, $n_1 = \langle n_1\rangle + \delta n$ with $\langle\delta n\rangle = \langle\delta\phi\rangle = 0$. The flux-surface average is calculated by $\langle\phi\rangle \equiv \frac{\oint d\theta d\zeta J\phi}{\oint d\theta d\zeta J}$. Subtracting Eq. (7) by its flux-surface average gives

$$\delta\phi - \delta\tilde{\phi} + \langle\tilde{\phi}\rangle - \langle\tilde{\phi}\rangle = \frac{T_i e}{n_i z_i{}^2}(z_i\delta\bar{n}_i - \delta n_e). \tag{10}$$

In the large aspect ratio limit, the term $\langle\tilde{\phi}\rangle - \langle\tilde{\phi}\rangle$ in the preceding equation mainly represents the coupling between the equilibrium magnetic field and $\phi_{n=0,m\neq 0}$ harmonics, which is transparent in the long wavelength limit $\langle\tilde{\phi}\rangle - \langle\tilde{\phi}\rangle = (k_r{}^2\rho_i{}^2 - \langle k_r{}^2\rho_i{}^2\rangle)\langle\phi\rangle - \langle k_\perp{}^2\rho_i{}^2\delta\phi\rangle \approx -\langle k_\perp{}^2\rho_i{}^2\delta\phi\rangle$. If we assume the equilibrium magnetic field takes the form $B = \sum_{m=0}^{\infty}(A_m\varepsilon^m\cos^m\theta + B_m\varepsilon^m\sin^m\theta)$ with $\varepsilon = r/R_0$ as the inverse aspect ratio, then it can be estimated with $(\langle\tilde{\phi}\rangle - \langle\tilde{\phi}\rangle)_{n=0,m\neq 0} \sim \varepsilon^m\delta\phi_{n=0,m\neq 0}$, which is usually much smaller than $(\delta\phi - \tilde{\delta}\phi)_{n=0,m\neq 0}$ for tokamaks. Therefore, the following gyrokinetic Poisson equation can be used to compute the fluctuating potential with the requisite accuracy:

$$\delta\phi - \tilde{\delta}\phi = \frac{T_i e}{n_i z_i{}^2}(z_i\delta\bar{n}_i - \delta n_e). \tag{11}$$

The flux-surface averaged gyrokinetic Poisson equation using Eqs. (7) and (9) can be written as

$$\langle\nabla_\perp^2\phi\rangle = \left\langle\left(\frac{T_i}{\rho_i{}^2 n_i z_i{}^2} - \frac{T_i}{n_i Z_i{}^2}\nabla_\perp{}^2\right)e(n_{e1} - Z_i\bar{n}_{i1})\right\rangle. \tag{12}$$

Using Eq. (16), the flux-surface averaged perpendicular Laplacian $\langle\nabla_\perp^2\phi\rangle$ in the preceding equation can be evaluated by

$$\langle\nabla_\perp^2\phi\rangle = \frac{1}{J_0(\psi)}\left[\frac{\partial}{\partial\psi}\left(J_0(\psi)\langle g^{\psi\psi}\rangle\frac{\partial\langle\phi\rangle}{\partial\psi}\right) + \frac{\partial J_0(\psi)}{\partial\psi}\left\langle g^{\psi\psi}\frac{\partial\delta\phi}{\partial\psi}\right\rangle + \frac{\partial J_0(\psi)}{\partial\psi}\left\langle g^{\psi\theta}\frac{\partial\delta\phi}{\partial\theta}\right\rangle\right], \tag{13}$$

where $J_0(\psi) = \oint d\theta d\zeta J$ is the flux-surface averaged Jacobian. The ratio between the second and the first terms is $\varepsilon\delta\phi_{m=1}/\langle\phi\rangle \ll 1$, i.e., negligible in the large-aspect-ratio limit. The third term is even smaller than the second by the factor $g^{\psi\theta}/g^{\psi\psi}$, where $g^{\psi\theta}$ measures the non-orthogonality of the magnetic coordinates (ψ,θ), which might be small for most flux surfaces in a tokamak. Therefore, we only keep the first term on the right-hand side of Eq. (13). If we let $\rho_c = e(Z_i\bar{n}_{i1} - n_{e1})$, then the gyrokinetic Poisson equation for the zonal potential $\langle\phi\rangle$ reads as follows:

$$\frac{\partial}{\partial\psi}\left(J(\psi)\langle g^{\psi\psi}\rangle\frac{\partial\langle\phi\rangle}{\partial\psi}\right) = \left(-\frac{T_i}{n_i Z_i{}^2}J(\psi)\left\langle\frac{1}{\rho_i{}^2}\right\rangle + \frac{T_i}{n_i Z_i{}^2}\frac{\partial}{\partial\psi}J(\psi)\langle g^{\psi\psi}\rangle\frac{\partial}{\partial\psi}\right)\langle\rho_c\rangle. \tag{14}$$

We integrate the preceding equation to obtain the zonal electric field

$$\frac{\partial\langle\phi\rangle}{\partial\psi} = -\frac{T_i}{n_i Z_i{}^2}\frac{\partial\langle\rho_c\rangle}{\partial\psi} - \frac{1}{J(\psi)\langle g^{\psi\psi}\rangle}\int_{\psi_0}^{\psi} d\psi\frac{T_i J(\psi)}{n_i Z_i{}^2} \times\left(\left\langle\frac{1}{\rho_i{}^2}\right\rangle + \langle g^{\psi\psi}\rangle\frac{d\ln(T_i/n_i)}{d\psi}\frac{\partial}{\partial\psi}\right)\langle\rho_c\rangle. \tag{15}$$

The preceding equation has been used in the GTC to calculate the zonal flow response for a given density perturbation, which has reproduced the Rosenbluth–Hinton residual level.[33]

IV. LAPLACIAN OPERATOR AND GEOMETRIC TENSOR

The inversion of the Laplacian operator plays a crucial role in computing perturbed electromagnetic fields. In this section, we study how to discretize the Laplacian operator in magnetic coordinates using the finite difference method. In the magnetic coordinate system, the Laplacian can be expressed as

$$\nabla^2 f = \frac{1}{J}\frac{\partial}{\partial\xi^\alpha}\left(J\nabla\xi^\alpha\cdot\nabla\xi^\beta\frac{\partial}{\partial\xi^\beta}f\right), \quad \text{with } \alpha = 1,2,3, \text{ and } \beta = 1,2,3, \tag{16}$$

where $(\xi^1,\xi^2,\xi^3) = (\psi,\theta,\zeta)$ are the coordinates of the Jacobian $J = (\nabla\psi\cdot\nabla\theta\times\nabla\zeta)^{-1}$. We define a contravariant geometric tensor $g^{\xi^\alpha\xi^\beta} \equiv \nabla\xi^\alpha\cdot\nabla\xi^\beta$. For an axisymmetric system, the Laplacian can be explicitly expressed as

$$\nabla^2 f = g^{\psi\psi}\frac{\partial^2 f}{\partial\psi^2} + 2g^{\psi\theta}\frac{\partial^2 f}{\partial\psi\partial\theta} + g^{\theta\theta}\frac{\partial^2 f}{\partial\theta^2} + g^{\zeta\zeta}\frac{\partial^2 f}{\partial\zeta^2} + \frac{1}{J}\left(\frac{\partial Jg^{\psi\psi}}{\partial\psi} + \frac{\partial Jg^{\psi\theta}}{\partial\theta}\right)\frac{\partial f}{\partial\psi} + \frac{1}{J}\left(\frac{\partial Jg^{\psi\theta}}{\partial\psi} + \frac{\partial Jg^{\theta\theta}}{\partial\theta}\right)\frac{\partial f}{\partial\theta}. \tag{17}$$

To compute the above Laplacian, we first need to compute the contravariant geometric tensor $g^{\xi^\alpha\xi^\beta}$. The B-spline representation of the magnetic field provides a transformation between two coordinate systems, i.e., $X = X(\psi,\theta)$ and $Z = Z(\psi,\theta)$, where (X,Z,ζ) are the toroidal coordinates. The covariant geometric tensor $g_{\xi^\alpha\xi^\beta}$ can be obtained by the following formula:

$$g_{\psi\psi} = \left(\frac{\partial X}{\partial\psi}\right)^2 + \left(\frac{\partial Z}{\partial\psi}\right)^2, \tag{18}$$

$$g_{\theta\theta} = \left(\frac{\partial X}{\partial\theta}\right)^2 + \left(\frac{\partial Z}{\partial\theta}\right)^2, \tag{19}$$

$$g_{\psi\theta} = \frac{\partial X}{\partial \psi}\frac{\partial X}{\partial \theta} + \frac{\partial Z}{\partial \psi}\frac{\partial Z}{\partial \theta}, \tag{20}$$

and $g_{\theta\psi} = g_{\psi\theta}, g_{\zeta\zeta} = X^2$. Using the identity $g_{\xi^\alpha\xi^\beta}g^{\xi^\beta\xi^\gamma} = \delta^\gamma_\alpha$, we can find the transformation from the covariant to contravariant geometric tensor, i.e.,

$$\begin{bmatrix} g^{\psi\psi} & g^{\psi\theta} & 0 \\ g^{\theta\psi} & g^{\theta\theta} & 0 \\ 0 & 0 & g^{\zeta\zeta} \end{bmatrix} = \begin{bmatrix} g_{\theta\theta} & -g_{\psi\theta} & 0 \\ -g^{\theta\psi} & g_{\psi\psi} & 0 \\ 0 & 0 & \Delta/g_{\zeta\zeta} \end{bmatrix} \frac{1}{\Delta}, \tag{21}$$

with the determinant $\Delta = g_{\psi\psi}g_{\theta\theta} - g_{\theta\psi}g_{\psi\theta}$.

Closely related to the magnetic coordinates, the field-aligned coordinates $(\psi, \theta_0, \zeta_0)$ are used in the GTC code to define the field-aligned mesh, which is essential for reducing the number of toroidal grids, where $\theta_0 = \theta - \zeta/q$ and $\zeta_0 = \zeta$. Then, the Laplacian in this new coordinate system becomes

$$\nabla^2 f = g^{\psi\psi}\frac{\partial^2 f}{\partial \psi^2} + 2g^{\psi\theta}\frac{\partial^2 f}{\partial \psi \partial \theta_0} + g^{\theta\theta}\frac{\partial^2 f}{\partial \theta_0{}^2} + g^{\zeta\zeta}\left(\frac{\partial}{\partial \zeta_0} - \frac{\partial}{q\partial\theta_0}\right)^2 f + \frac{1}{J}\left(\frac{\partial J g^{\psi\psi}}{\partial \psi} + \frac{\partial J g^{\psi\theta}}{\partial \theta_0}\right)\frac{\partial f}{\partial \psi} + \frac{1}{J}\left(\frac{\partial J g^{\psi\theta}}{\partial \psi} + \frac{\partial J g^{\theta\theta}}{\partial \theta_0}\right)\frac{\partial f}{\partial \theta_0}. \tag{22}$$

Using the fact that the perpendicular scale length is much shorter than the parallel scale length, the perpendicular Laplacian can be obtained from the preceding equation:

$$\nabla_\perp{}^2 f = g^{\psi\psi}\frac{\partial^2 f}{\partial \psi^2} + 2g^{\psi\theta}\frac{\partial^2 f}{\partial \psi \partial \theta_0} + \left(g^{\theta\theta} + g^{\zeta\zeta}/q^2\right)\frac{\partial^2 f}{\partial \theta_0{}^2} + \frac{1}{J}\left(\frac{\partial J g^{\psi\psi}}{\partial \psi} + \frac{\partial J g^{\psi\theta}}{\partial \theta_0}\right)\frac{\partial f}{\partial \psi} + \frac{1}{J}\left(\frac{\partial J g^{\psi\theta}}{\partial \psi} + \frac{\partial J g^{\theta\theta}}{\partial \theta_0}\right)\frac{\partial f}{\partial \theta_0}. \tag{23}$$

Next, we study how to discretize the preceding perpendicular Laplacian. In the GTC code, we use an unstructured mesh to ensure an approximately equal grid size in the radial and poloidal directions. The mesh grids are uniform in the θ_0 direction for each flux surface and nonuniform in the ψ direction. To evaluate the Laplacian numerically in Eq. (23), we need to discretize the following five operators: $\frac{\partial}{\partial \theta_0}$, $\frac{\partial}{\partial \psi}$, $\frac{\partial^2}{\partial \psi^2}$, $\frac{\partial^2}{\partial \psi \partial \theta_0}$, and $\frac{\partial^2}{\partial \theta_0{}^2}$. The discretization of these differential operators using the finite difference method is shown in Appendix C. We note here that in the GTC code, the gyrokinetic Poisson equation is solved in the field-aligned coordinates, while the particles are pushed in magnetic coordinates, as shown in Appendix B. To evaluate the electric field in the particle-pushing procedure, we need to use the following transformation: $\frac{\partial \phi}{\partial \theta} = \frac{\partial \phi}{\partial \theta_0}, \frac{\partial \phi}{\partial \zeta} = \frac{\partial \phi}{\partial \zeta_0} - \frac{1}{q}\frac{\partial \phi}{\partial \theta_0}$.

After discretizing each term in Eq. (23), we can convert the Poisson equation $\nabla_\perp{}^2\phi = \delta n(\psi, \theta)$ to a big matrix equation and solve it parallelly using the software of PETSc.[34] A numeric example is provided to verify the numerical Poisson solver. In the simple circular cross section limit, we assume the safety factor $q = \text{const}$, then $g^{\psi\psi} = r^2/q^2$, $g^{\theta\theta} = 1/r^2$, $g^{\psi\theta} = 0$, and $g^{\zeta\zeta} = 1/X^2$ with $X = 1 + r\cos\theta/R_0$. Then, the Laplace operator including the essential toroidal effect in the field-aligned coordinates becomes $\nabla_\perp{}^2 = \frac{\partial^2}{\partial r^2} + \left(\frac{1}{r} + \frac{\cos\theta_0}{X}\right)\frac{\partial}{\partial r} + \left(\frac{1}{r^2} + \frac{1}{q^2X^2}\right)\frac{\partial^2}{\partial \theta_0{}^2} - \frac{\sin\theta_0}{Xr}\frac{\partial}{\partial \theta_0}$. The source term in the Poisson equation is set as $\delta n(r, \theta_0) = \nabla_\perp{}^2\left[\sin\left(4\pi\frac{r-a_0}{a_1-a_0}\right)\cos(m\theta_0)\right]$ with $m = 6$, which is shown in Fig. 5(a) in the 2D poloidal plane. Using the boundary condition $\phi(r = a_0) = \phi(r = a_1) = 0$ and the new Poisson solver implemented in the GTC, we can find the numeric solution to the Poisson equation, as shown in Fig. 5(b). Then, we find the numeric values along the black solid line in Fig. 5(b) and compare

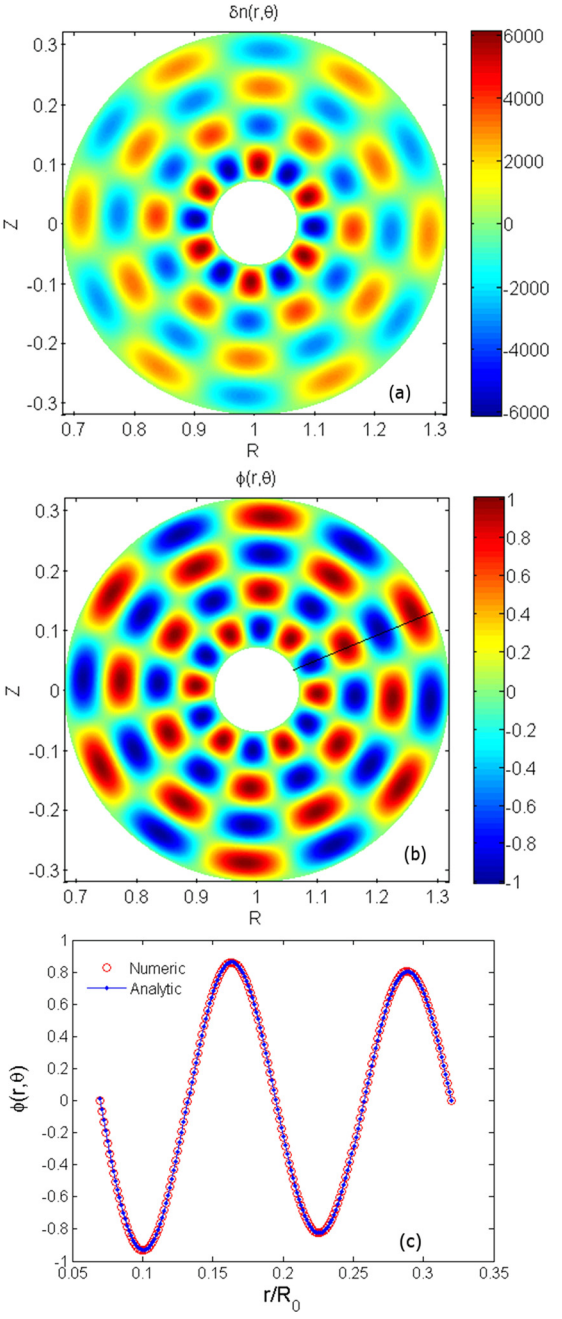

FIG. 5. Verification of Poisson solver. Verification of Poisson solver by solving Poisson equation $\nabla_\perp{}^2\phi = \delta n$ analytically and numerically. (a) 2D contour for the source term $\delta n(r, \theta)$, (b) 2D contour for the numerical solution $\phi(r, \phi)$ to Poisson equation, (c) comparison between the numerical and analytical solutions along the black line in (b).

them with those from the analytic solution. As shown in Fig. 5(c), the numeric solution almost overlaps the analytic solution, which verifies the effectiveness of this finite-difference-based Poisson solver.

V. SIMULATION FOR DIII-D EXPERIMENT

Next, we compile all the newly developed features in the GTC to simulate a real tokamak experiment based on the DIII-D discharge #101391.[26] This low-β L-mode discharge has been carefully studied by the GYRO code.[25] Therefore, the simulation of this particular discharge provides a useful benchmark case for the verification of the gyrokinetic codes through completely different approaches. To undertake a meaningful verification/validation, it is critical to compare the conventions used in these codes. We first compare the convention of the input physical quantities in the GTC with that of GYRO in Appendix D. Then, we use the GTC to perform an electrostatic turbulence simulation with kinetic electrons. The temperature and density profiles for ions and electrons are taken from the EFIT-produced iterdb file. Figure 6 shows the input profiles for the GTC simulation for the domain $r \subset [0.12a, 0.82a]$. As the zero boundary condition is assumed in the GTC simulation, we artificially flatten the plasma profiles at the two edges of the simulation domain to lower the turbulence drive in those regions.

Generally, in the PIC simulation, a limited number of particles are used to simulate a physical system; these particles are called "markers." For the background marker loading at the beginning of the simulation, we apply two different methods: uniform and nonuniform loading. For the uniform loading method, the marker temperature and density are set to be uniform along the radial direction, which is equal to the value at reference point $r = r_{ref}$, while still maintaining the experimental temperature and density gradient profiles, as sketched in Figs. 7(a) and 7(b). For the nonuniform loading method, we choose the marker temperature and density to follow faithfully the input profiles and their gradients, as shown by Figs. 7(c) and 7(d). Conventionally, the GTC uses the uniform loading method because it has less Monte-Carlo noise than the nonuniform loading method for the same total number of particles in the simulation. As discussed in Sec. III, the gyrokinetic Poisson equation can also be solved using two approaches: the improved four-point average method or the Pade approximation method.

We show the time history of the volume-averaged ion heat diffusivity in Fig. 8, in which the red solid line denotes uniform loading and the line of red circles denotes nonuniform loading. In these two cases, the improved four-point average method is used to solve the gyrokinetic Poisson equation. The line of blue squares in Fig. 8 shows the time history of the ion heat diffusivity for nonuniform loading using the Pade approximation to solve the gyrokinetic Poisson equation. Each of these three methods provides the same level of turbulent transport, which indicates that the uniform loading method is a good approximation to the essential turbulent transport physics. Furthermore, it confirms that the Pade approximation is as good as the four-point average method in solving the gyrokinetic Poisson equation in the turbulence simulation.

Then, we focus on the gyrokinetic simulation using nonuniform marker loading and the improved four-point Poisson solver. The 3D global turbulence mode structure is displayed for the linear and nonlinear stages in Figs. 9(a) and 9(b),

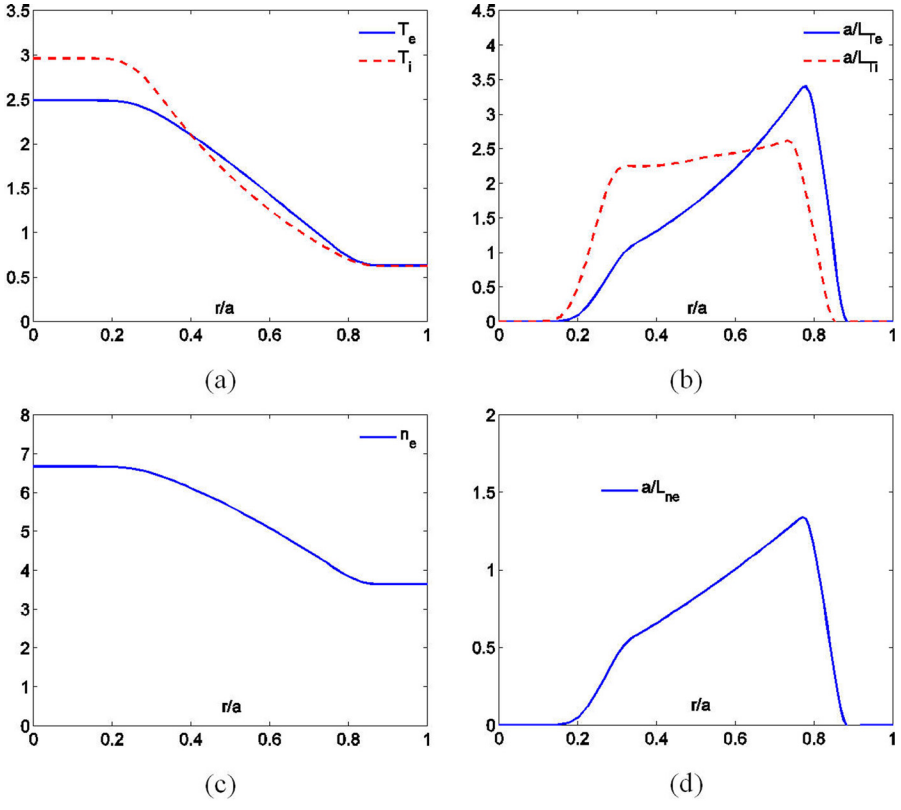

FIG. 6. Radial profiles for the DIII-D discharge #101391. Radial profiles from the GTC for the following equilibrium quantities: (a) electron and ion temperature, (b) electron and ion temperature gradient, (c) electron density, and (d) electron density gradient.

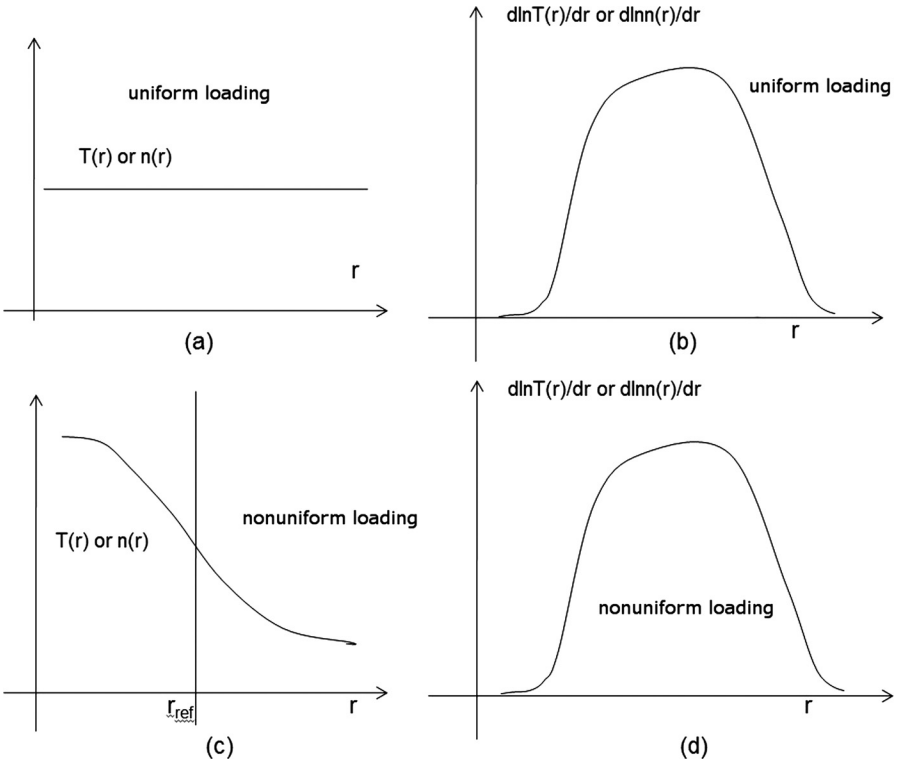

FIG. 7. Background plasma profile setting. Sketch of loading scheme of the background particle distribution in the GTC simulation: (a) and (b) uniform loading: uniform radial profiles for marker temperature and density with real/nonuniform temperature and density gradients to excite instability; (c) and (d) nonuniform loading: real/nonuniform radial profiles for marker temperature and density with real/nonuniform temperature and density gradients to excite instability. For uniform loading, the temperature/density in (a) is set as the value at reference point $r = r_{ref}$ in (c).

respectively. In the linear stage, an eigenmode structure forms along the radial direction. The real frequency of the eigenmode is in the ion diamagnetic direction, which shows that it is an ITG instability. In the nonlinear stage, because of the excitation of the zonal flow, the predominant linear radial structure is totally destroyed. This confirms that the zonal flow plays an important role in regulating turbulence for this particular case.

The ion heat diffusivity is time-averaged during the nonlinear stage at each radial location, which gives the radial profile of the time-averaged ion heat diffusivity, as shown by the solid red line in Fig. 10. As a comparison, the ion heat diffusivity profile from the GYRO simulation is also represented by the dashed line in Fig. 10.[26] These two curves

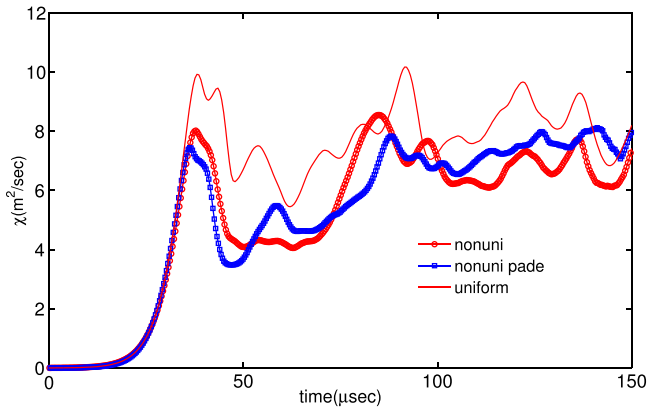

FIG. 8. Time history of ion heat diffusivity. Time history of the ion heat diffusivity for three different cases. Uniform means uniform marker loading with improved four-point average method to solve gyrokinetic Poisson equation, nonuni means nonuniform marker loading with improved four-point average method, and nonuni pade means nonuniform marker loading with Pade approximation to solve gyrokinetic Poisson equation.

overlap each other very well, which provides good verification in the microturbulence simulation between the two different gyrokinetic codes.

The results are then shown for the simulation that uses the Pade approximation to solve the gyrokinetic Poisson equation. The radial profiles of the time-averaged ion and electron heat diffusivity are shown by the dashed lines in Fig. 11. In this figure, the time-averaged ion and electron heat diffusivity from the improved four-point average method are also represented by the solid lines. These two different methods for solving the gyrokinetic equation provide approximately similar radial profiles for the ion and electron heat diffusivity. Therefore, either of these two methods would be applicable for a large aspect ratio tokamak. However, the four-point average method relies on the fact that the poloidal plane is very close to the perpendicular plane, which is valid only in the large aspect ratio tokamak. Therefore, the four-point average method might not be accurate for small aspect ratio tokamaks such as the NSTX, whereas the Pade approximation would remain applicable.

Next, we compare the radial profiles for the time-averaged ion heat diffusivity for the two marker loading methods mentioned earlier. In Fig. 12, the solid line represents nonuniform loading and the dashed line stands for uniform loading. It can be seen that the ion heat diffusivity from uniform loading is larger on the inner side than that from nonuniform loading. However, on the outer side of the radius, the ion heat diffusivity for uniform loading is smaller. This phenomenon may be explained by the fact that on the inner side of the radius, the marker temperature and thus the ion gyroradius for nonuniform loading is larger than for uniform loading. Because of the stabilizing effect of the gyroaverage, i.e., the FLR effect, the linear drive and

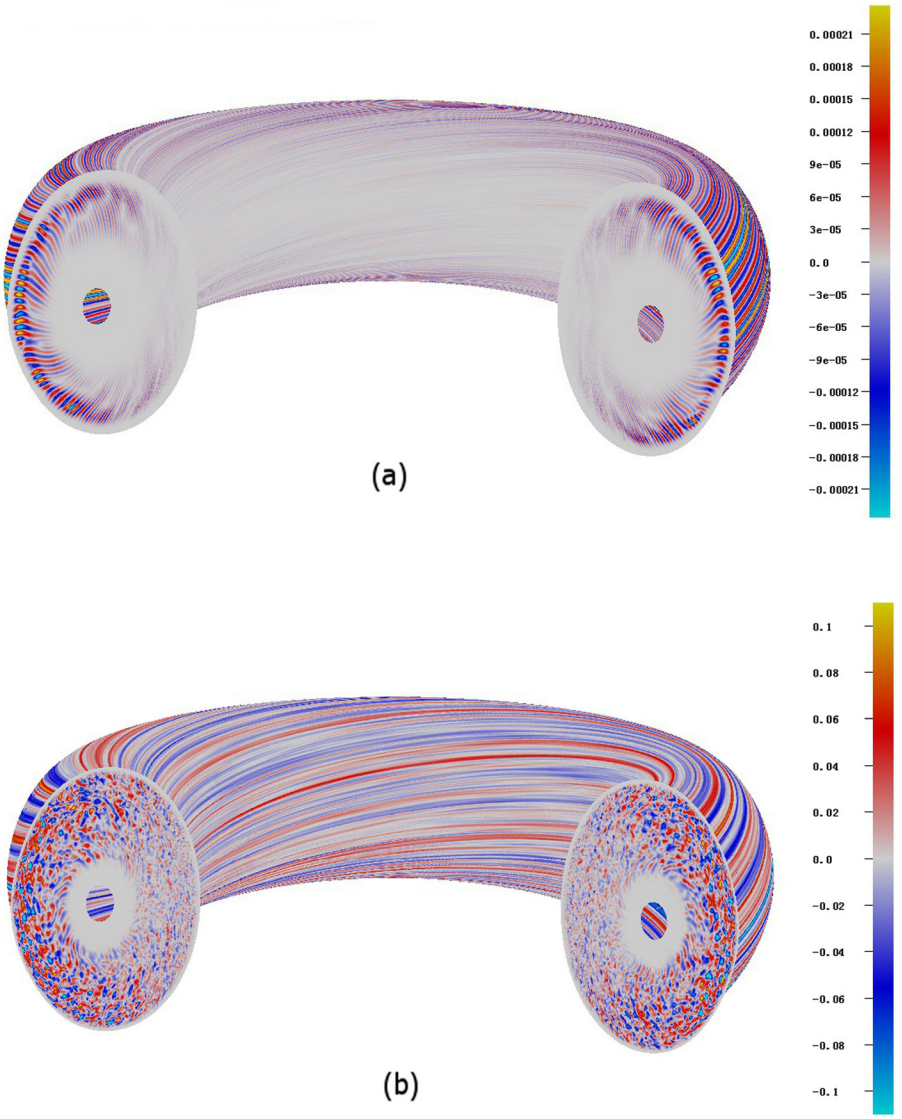

FIG. 9. Three-dimensional contour of turbulence structure. Gyrokinetic simulation of the DIII-D discharge #101391 showing global mode structure in: (a) linear growth stage and (b) nonlinear stage.

associated turbulent transport for nonuniform loading is smaller than for uniform loading on the inner side of the radius. The same argument could be applied to explain why the turbulent transport on the outer side is smaller for uniform loading than for nonuniform loading.

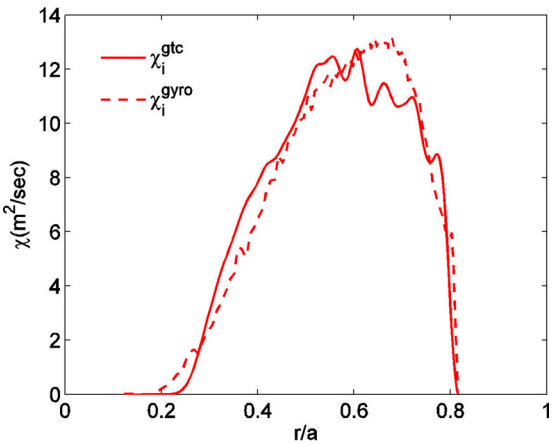

FIG. 10. Radial profile of ion heat diffusivity. Comparison of radial profiles of ion heat diffusivity from the GTC and GYRO simulations.

VI. SUMMARY AND DISCUSSION

In this paper, we extended the GTC code to import experimental profiles and magnetic geometry for the simulation of turbulent transport in general geometry using B-splines to

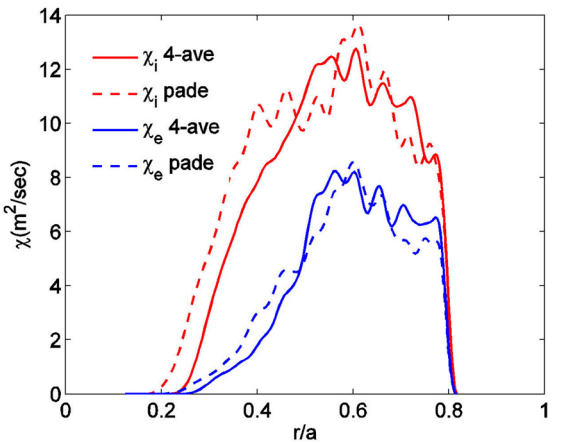

FIG. 11. Heat diffusivity radial profiles from four-point average method and Pade approximation. Time-averaged heat diffusivity radial profiles from four-point average (4-ave) method and Pade approximation.

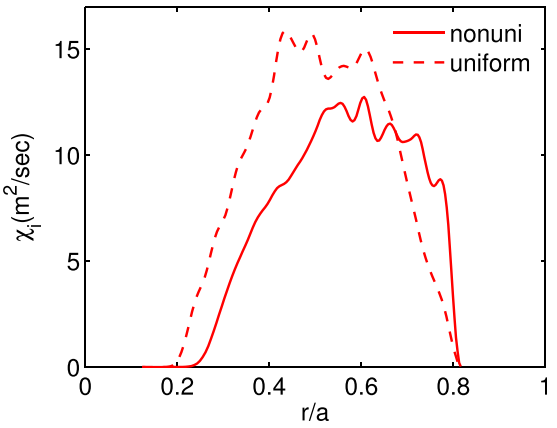

FIG. 12. Heat diffusivity radial profiles for the two methods of marker loading. Heat diffusivity radial profiles for the two different methods of marker loading. Uniform means uniform marker loading and nonuni means nonuniform marker loading.

interpolate the equilibrium data. A new Poisson solver based on flux coordinates and the finite difference scheme was designed and successfully implemented in the GTC, which can be used in conjunction with the Pade approximation to solve the gyrokinetic Poisson equation. This new Poisson solver could also be used for electromagnetic simulations. We also improved the conventional four-point average method to include higher-order global effects for the gyrokinetic Poisson equation. An electrostatic turbulence simulation was performed for the DIII-D discharge #101391 using these two different approaches for the gyrokinetic Poisson equation. The resultant turbulent transport levels were found to be consistent with each other. The radial profile of the heat diffusivity was compared with that from GYRO and good agreement was found. For the background marker loading, we developed and tested a nonuniform loading method and found only a small difference from the conventional uniform loading method for the volume-averaged turbulent transport. However, on the radial structure, there was a nontrivial difference between the different loading methods. This difference could be attributed to the stabilizing effect of the gyroaverage (FLR effect). The new algorithm for solving the Poisson equation using the flux coordinates could be used for electromagnetic simulations, where Ampere's law has a similar Laplacian form. Another advantage of this new gyrokinetic Poisson solver is that it could be used to simulate small aspect ratio tokamaks, because the gyrokinetic Poisson equation is solved in the perpendicular plane rather than in the poloidal plane as in the conventional GTC simulation.

ACKNOWLEDGMENTS

This work was supported by the National Magnetic Confinement Fusion Science Program under Grant Nos. 2011GB105001, 2015GB110000, and 2013GB111000, China NSFC under Grant No. 91130031, the Recruitment Program of Global Youth Experts, U.S. DOE SciDac GSEP centers. One of the authors (Y. Xiao) would like to thank R. Waltz for providing the DIII-D data, and C. Holland and D. Liu for useful discussions.

APPENDIX A: B-SPLINE INTERPOLATION

Generally, two classes of function are involved in describing the magnetic geometry and plasma profiles in axisymmetric systems such as tokamaks: a 1D function $f(\psi)$ and a 2D function. For the 1D function $f(\psi)$, such as the ion temperature profile $T_i(\psi)$ and toroidal current $g(\psi)$, we can use the following B-spline representation:

$$f(\psi) = f(1,i) + f(2,i)h + f(3,i)h^2, \tag{A1}$$

where $\psi_i \le \psi < \psi_{i+1}, h = \psi_{i+1} - \psi_i, i = 0, 1, ..., N,$ and $f(1,i) = f(\psi_i)$. Here, we assume uniform grid size in the radial direction. The coefficients $f(2,i)$ and $f(3,i)$ can be calculated from $f(1,i)$. Using the zeroth and first-order continuous conditions for the 1D function $f(\psi)$

$$f(x_i + h) = f(x_{i+1}), f'(x_i + h) = f'(x_{i+1}), \tag{A2}$$

we find that

$$f(1,i+1) = f(1,i) + f(2,i)h + f(3,h)h^2, \tag{A3}$$

$$f(2,i+1) = f(2,i) + 2f(3,i)h. \tag{A4}$$

The preceding two iterative equations are used to obtain the B-spline coefficients: $f(2,i)$ and $f(3,i)$. However, the two initial values of $f(2,1)$ and $f(3,1)$ remain to be determined, which it relies on the specific features of the 1D function $f(\psi)$ around the initial point ψ_0. When $\psi \to \psi_0$, there are four relevant cases to be considered.

Case 1: $f(\psi) = a + b\Delta\psi$, where $\Delta\psi \equiv \psi - \psi_0$. In this case, the coefficients $f(2,1)$ and $f(3,1)$ are found to be

$$f(2,1) = [f(1,2) - f(1,1)]/h \tag{A5}$$

and

$$f(3,1) = 0. \tag{A6}$$

Case 2: $f(\psi) = a + b\Delta\psi^2$, in which the coefficients $f(2,1)$ and $f(3,1)$ are found to be

$$f(2,1) = 0 \tag{A7}$$

and

$$f(3,1) = [f(1,2) - f(1,1)]/h^2. \tag{A8}$$

Case 3: $f(\psi) = a + b\Delta\psi + c\Delta\psi^2$, in which the coefficients $f(2,1)$ and $f(3,1)$ are found to be

$$f(2,1) = [4f(1,2) - f(1,3) - 3f(1,1)]/(2h) \tag{A9}$$

and

$$f(3,1) = [f(1,2) - f(1,1) - f(2,1)h]/h^2. \tag{A10}$$

Case 4: $f(x) = a + b\sqrt{\Delta\psi} + c\Delta\psi$. This case needs special care to find a smooth $f(1,i)$ and the iteration equations become

$$f(2,i) = -f(2,i-1) + 2[f(1,i) - f(1,i-1)]/h, \tag{A11}$$

$$f(1,i+1) = f(2,i)/(2h) + f(1,i+2)/4 + 3f(1,i)/4, \tag{A12}$$

and

$$f(3,i) = [f(2,i+1) - f(2,i)]/2h. \tag{A13}$$

To evolve the preceding equations, the initial coefficients $f(2,1)$ and $f(3,1)$ are found to be

$$f(2,1) = [2f(1,2) - f(1,3) - f(1,1)]/\left[(2-\sqrt{2})\sqrt{h}\right] \tag{A14}$$

and

$$f(3,1) = \left[f(1,2) - f(1,1) - f(2,1)\sqrt{h}\right]/h, \tag{A15}$$

and the initial coefficients $f(2,2)$ and $f(3,2)$ are found to be

$$f(2,2) = f(3,1) + f(2,1)/(2\sqrt{h}) \tag{A16}$$

and

$$f(3,2) = [f(1,3) - f(1,2) - hf(2,2)]/h^2. \tag{A17}$$

The end point also needs special treatment

$$f(2,N-1) = -f(2,N-2) + 2[f(1,N-1) - f(1,N-2)]/h. \tag{A18}$$

We note that with the above settings, the inversion of these B-spline functions can also be obtained.

After constructing 1D B-splines, the derivative of the spline function can easily be found as

$$f'(\psi_i) = f(2,i) + 2hf(3,i). \tag{A19}$$

This expression is useful for evaluating the temperature gradient $dT(\psi)/d\psi$ and density gradient $dn(\psi)/d\psi$, which are the main instability drives for the microturbulence.

Once these 1D spline functions are constructed, we can proceed to construct the B-spline functions for one class of very useful 2D functions $f(\psi,\theta) = \sum_n g_n(\psi)h_n(\theta)$, which can be used to describe most tokamak equilibrium magnetic configurations. Each function $g_n(\psi)$ or $h_n(\theta)$ can be represented by the 1D B-splines, i.e., $g_n(\psi) = g_n(i,1) + g_n(i,2)\Delta\psi + g_n(i,3)\Delta\psi^2$ and $h_n(\psi) = h_n(i,1) + h_n(i,2)\Delta\theta + h_n(i,3)\Delta\theta^2$. Then, the 2D function $f(\psi,\theta)$ can be expressed by the following equation to the accuracy of the second order:

$$\begin{aligned} f(\psi,\theta) =& f(1,i,j) + f(2,i,j)\Delta\psi + f(3,i,j)\Delta\psi^2 \\ &+ f(4,i,j)\Delta\theta + f(5,i,j)\Delta\psi\Delta\theta + f(6,i,j)\Delta\theta\Delta\psi^2 \\ &+ f(7,i,j)\Delta\theta^2 + f(8,i,j)\Delta\psi\Delta\theta^2 + f(9,i,j)\Delta\psi^2\Delta\theta^2, \end{aligned} \tag{A20}$$

where the coefficients $f(m,i,j)$, $m = 1,...,9$, can be related by the spline coefficients $g_n(i,l)$ and $h_n(i,l)$. The derivatives of $f(\psi,\theta)$ on the grid points, to the accuracy of first order, can be found as

$$\begin{aligned} f_\psi(\psi,\theta) =& f(2,i,j) + f(5,i,j)\Delta\theta + f(8,i,j)\Delta\theta^2 \\ &+ 2\Delta\psi[f(3,i,j) + f(6,i,j)\Delta\theta + f(9,i,j)\Delta\theta^2], \end{aligned} \tag{A21}$$

$$\begin{aligned} f_\theta(\psi,\theta) =& f(4,i,j) + f(5,i,j)\Delta\psi + f(6,i,j)\Delta\psi^2 \\ &+ 2\Delta\theta[f(7,i,j) + f(8,i,j)\Delta\psi + f(9,i,j)\Delta\psi^2]. \end{aligned} \tag{A22}$$

These expressions are particularly useful for calculating relevant physical quantities such as $\partial B/\partial\psi$ and $\partial B/\partial\theta$, which will be used to compute the particle motion in the gyrokinetic simulation.

APPENDIX B: EQUATION OF MOTION IN BOOZER COORDINATES

The original equation of motion in Boozer coordinates[35] can be applied to the general magnetic geometry case. For completeness, we list these equations of motion implemented in the GTC for the electrostatic simulation

$$\dot{\zeta} = \frac{\bar{\rho}_\parallel \bar{B}^2}{\bar{D}}\left(q + \bar{\rho}_\parallel \bar{I}'\right) - \frac{1}{Z_\alpha}\left(\bar{\mu} + \frac{Z_\alpha{}^2}{\bar{m}_\alpha}\bar{\rho}_\parallel{}^2\bar{B}\right)\frac{\bar{I}}{\bar{D}}\frac{\partial\bar{B}}{\partial\bar{\psi}} - \frac{\bar{I}}{\bar{D}}\frac{\partial\bar{\phi}}{\partial\bar{\psi}}, \tag{B1}$$

$$\dot{\theta} = \frac{\bar{\rho}_\parallel \bar{B}^2}{\bar{D}}\left(1 - \bar{\rho}_\parallel \bar{g}'\right) + \frac{1}{Z_\alpha}\left(\bar{\mu} + \frac{Z_\alpha{}^2}{\bar{m}_\alpha}\bar{\rho}_\parallel{}^2\bar{B}\right)\frac{\bar{g}}{\bar{D}}\frac{\partial\bar{B}}{\partial\bar{\psi}} + \frac{\bar{g}}{\bar{D}}\frac{\partial\bar{\phi}}{\partial\bar{\psi}}, \tag{B2}$$

$$\begin{aligned} \dot{\bar{\psi}} =& -\frac{1}{Z_\alpha}\frac{\bar{g}}{\bar{D}}\left(\bar{\mu} + \frac{Z_\alpha{}^2}{\bar{m}_\alpha}\bar{\rho}_\parallel{}^2\bar{B}\right)\frac{\partial\bar{B}}{\partial\theta} \\ &+ \frac{1}{Z_\alpha}\frac{\bar{I}}{\bar{D}}\left(\bar{\mu} + \frac{Z_\alpha{}^2}{\bar{m}_\alpha}\bar{\rho}_\parallel{}^2\bar{B}\right)\frac{\partial\bar{B}}{\partial\zeta} + \frac{\bar{I}}{\bar{D}}\frac{\partial\bar{\phi}}{\partial\zeta} - \frac{\bar{g}}{\bar{D}}\frac{\partial\bar{\phi}}{\partial\bar{\psi}}, \end{aligned} \tag{B3}$$

$$\begin{aligned} \dot{\bar{\rho}}_\parallel =& -\frac{1}{Z_\alpha}\frac{\left(1 - \bar{\rho}_\parallel\bar{g}'\right)\left(\bar{\mu} + \frac{Z_\alpha{}^2}{\bar{m}_\alpha}\bar{\rho}_\parallel{}^2\bar{B}\right)}{\bar{D}}\frac{\partial\bar{B}}{\partial\theta} - \frac{\left(1 - \bar{\rho}_\parallel\bar{g}'\right)}{\bar{D}}\frac{\partial\bar{\phi}}{\partial\theta} \\ &- \frac{\left(\bar{q} + \bar{\rho}_\parallel\bar{I}'\right)}{\bar{D}}\frac{\partial\bar{\phi}}{\partial\zeta} - \frac{1}{Z_\alpha}\frac{\left(q + \bar{\rho}_\parallel\bar{I}'\right)\left(\bar{\mu} + \frac{Z_\alpha{}^2}{m_\alpha}\bar{\rho}_\parallel{}^2\bar{B}\right)}{\bar{D}}\frac{\partial\bar{B}}{\partial\zeta}. \end{aligned} \tag{B4}$$

This set of equations is based on a Hamiltonian principle with the guiding center Hamiltonian $H = \bar{\rho}_\parallel{}^2\bar{B}^2/2 + \bar{\mu}\bar{B} + \bar{\phi}$, which is suitable for determining the motion of the guiding centers of both ions and electrons. The physical quantities in the preceding equations are all normalized quantities: $\bar{\psi} = \frac{\psi}{B_0R_0{}^2}$, $\bar{\rho}_\parallel = \frac{\bar{v}_\parallel}{\Omega_\alpha} = \frac{v_\parallel}{R_0\Omega_\alpha}$, $\bar{D} = \frac{1}{B_0R_0}(qg + I + \bar{\rho}_\parallel(gI' - Ig'))$, $\bar{I} = \frac{I}{B_0R_0}$, $\bar{I}' = \frac{d\bar{I}}{d\bar{\psi}}$, $\bar{g} = \frac{g}{B_0R_0}$, $\bar{g}' = \frac{d\bar{g}}{d\bar{\psi}}$, $\bar{m}_\alpha = \frac{m_\alpha}{m_H}$, $\bar{\phi} = \frac{e\langle\phi\rangle_\varphi}{m_HR_0{}^2\Omega_0{}^2}$, where m_H is the hydrogen mass, $\Omega_0 = \frac{eB_0}{m_Hc}$ is hydrogen gyrofrequency, R_0 is the tokamak major radius, and B_0 is the magnetic field at the magnetic axis. However, we note in Ref. 35 that this set of equations is normalized by the particle gyrofrequency $\Omega_\alpha = \frac{Z_\alpha eB_0}{m_\alpha c}$. With some minor modifications, these equations of motion can also be used to push particles in the presence of electromagnetic perturbations.[13,35]

APPENDIX C: DISCRETIZATION OF DIFFERENTIAL OPERATOR ON THE GTC UNSTRUCTURED MESH

As the grid size in the θ_0 is uniform for each flux surface, we can apply a simple algorithm to discretize $\frac{\partial}{\partial\theta_0}$ to second-order accuracy

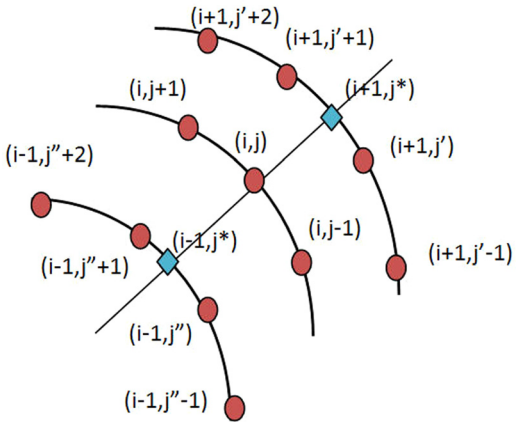

FIG. 13. Laplacian discretization. Discretization of Laplacian at mesh point (i, j) involves an additional 10 points around it.

$$\left(\frac{\partial f}{\partial \theta_0}\right)_{i,j} = \frac{f_{i,j+1} - f_{i,j-1}}{2(\Delta\theta_0)_i}, \tag{C1}$$

where i is the index label for ψ and j is the index label for θ_0, as shown in Fig. 13.

Then, we discretize $\frac{\partial}{\partial \psi}$ to obtain

$$\left(\frac{\partial f}{\partial \psi}\right)_{i,j} = w_2 \frac{f_{i+1,j*} - f_{i,j}}{h_2} + w_1 \frac{f_{i,j} - f_{i-1,j*}}{h_1}, \tag{C2}$$

with $h_1 = \psi_i - \psi_{i-1}$, $h_2 = \psi_{i+1} - \psi_i$ and $w_2 = h_1/(h_1 + h_2)$, $w_1 = h_2/(h_1 + h_2)$. The value of f_{i+1,j^*} can be evaluated using the neighboring four points on the same flux surface ψ_{i+1}, as shown in Fig. 13, to second-order accuracy

$$\begin{aligned} f_{i+1,j*} = {} & w_{i+1} f_{i+1,j'+1} + \lambda_{i+1} f_{i+1,j'} + \frac{\lambda_{i+1} w_{i+1}}{2} \\ & \left[w_{i+1} f_{i+1,j'+1} + \lambda_{i+1} f_{i+1,j'} - \frac{1}{3}(1 + w_{i+1}) f_{i+1,j'+2} \right. \\ & \left. - \frac{1}{3}(1 - \lambda_{i+1}) f_{i+1,j'-1} \right], \end{aligned} \tag{C3}$$

where $w_{i+1} = (\theta - \theta_{i+1,j'})/\Delta\theta_{i+1}$ and $\lambda_{i+1} = 1 - w_{i+1}$. A similar expression can be found for the value f_{i-1,j^*}.

We continue to discretize $\frac{\partial^2}{\partial\theta_0 \partial\psi}$ to obtain

$$\begin{aligned} \left(\frac{\partial^2 f}{\partial\theta_0 \partial\psi}\right)_{i,j} = {} & \left(\frac{w_1}{h_1} - \frac{w_2}{h_2}\right) \frac{f_{i,j+1} - f_{i,j-1}}{2\Delta\theta_i} + \frac{w_2}{h_2} \frac{\partial f_{i+1,j^*}}{\partial\theta_0} \\ & - \frac{w_2}{h_2} \frac{\partial f_{i-1,j^*}}{\partial\theta_0}. \end{aligned} \tag{C4}$$

Using the four neighboring points in the same flux surface, we can obtain

$$\begin{aligned} \frac{\partial f_{i+1,j^*}}{\partial\theta_0} = {} & \frac{1}{2\Delta\theta_{i+1}} \left[\lambda_{i+1} (f_{i+1,j'+1} - f_{i+1,j'-1}) \right. \\ & + w_{i+1} (f_{i+1,j'+2} - f_{i+1,j'}) + \frac{1}{3}(1 + 3\lambda_{i+1} w_{i+1}) \\ & \left. \times (f_{i+1,j'-1} - 3 f_{i+1,j'} + 3 f_{i+1,j'+1} - f_{i+1,j'+2}) \right]. \end{aligned} \tag{C5}$$

Similar expressions can be written for $\frac{\partial f_{i+1,j^*}}{\partial\theta_0}$. Finally, we deal with the operator $\frac{\partial^2}{\partial\psi^2}$

$$\left(\frac{\partial^2 f}{\partial\psi^2}\right)_{i,j} = \frac{2}{h_1 h_2} (w_1 f_{i-1,j^*} + w_2 f_{i+1,j^*} - f_{i,j}), \tag{C6}$$

where f_{i+1,j^*} can be evaluated by the four-point interpolation using Eq. (C3). A similar expression can be found for f_{i-1,j^*}.

APPENDIX D: CONVENTION ISSUES FOR THE GTC AND GYRO

The DIII-D discharge #101391 serves as a concrete example to discuss the differences between the GTC and GYRO. The GTC can create an analytic equilibrium based on a circular cross-sectional model or input a numerical equilibrium from EFIT data; the latter is usually used for precise comparison of experiments. All figures relating to the DIII-D discharge #101391 in this paper are taken from the GTC's output data and then translated to the GYRO convention if necessary. As shown in Fig. 14, each flux surface represents a particular value of the poloidal flux function $\psi = \psi(R, Z)$. The center of each flux surface ψ has the coordinates (R_0, Z_0), where $Z_0 \equiv \oint dZRZ / \oint dZR$ and $R_0 \equiv (R_+ - R_-)/2$ with R_- and R_+ being the intersection points of the flux surface and the horizontal line $Z = Z_0$. As shown by Fig. 14(a), the levitation of the flux surface center Z_0 is negligibly small for all flux surfaces. Starting from the flux surface center, we can define a set of new coordinates (r, θ), as shown in Fig. 15, which leads to $R_+ = R_0 + r(\psi, \theta = 0)$, $R_- = R_0 - r(\psi, \theta = \pi)$. Then, on the flux surface ψ, the effective radius in the GTC is set as $r \equiv r(\psi, \theta = 0) = R_+ - R_0$, which becomes a flux surface function. In the GYRO code, the effective radius r_g is defined slightly differently, i.e., $r_g \equiv [r(\psi, \theta = 0) + r(\psi, \theta = \pi)]/2 = (R_+ - R_-)/2$. The effective radiuses r_{gtc} and r_{gyro} are shown in Fig. 14(c) to vary with poloidal flux ψ. Another useful effective radial variable $\rho = \rho(\psi)$ is also used in the GYRO code, which has the definition $\psi_T = B_0 \rho^2/2$, where B_0 is the magnetic field at the magnetic axis. The toroidal magnetic flux ψ_T is related to the poloidal magnetic flux ψ by $d\psi_T/d\psi = q(\psi)$, where q is the safety factor. The quantity $\rho d\rho/(r_g dr_g)$, as shown in Fig. 14(d) for DIII-D discharge #101391, is important for determining the local effective magnetic field at the reference point, $B_{unit} = B_0 \frac{\rho d\rho}{r_g dr_g}$.[25] In the GYRO convention, the normalized gyroradius is $\rho_* = \rho_s/a$, where $\rho_s = c_s/\Omega_i$, and $c_s = \sqrt{T_e/m_i}$, and $\Omega_i = \frac{q_i B_{unit}}{c m_i}$. For the case of DIII-D discharge #101391, $R_0(0) = 1.72$m. According to Figs. 14 and 7, at the reference point $r_{gyro}/a = 0.60$, $R_0 = 0.98 R_0(0) = 1.69$m. In Fig. 14, we see that $a = 0.362 R_0(0) = 0.62$m. We can obtain $T_e = 1.2$kev at the reference point $r_g/a = 0.60$ from Fig. 6(a). In this discharge, $B_0 = 2.106T$ and at the reference point $B_{unit} = 3.085T$. These parameters give $\rho_s = 0.0017$m and then $\rho_s/a = 0.0027$. This value is the same as in Ref. 26. For a better comparison, we list some key parameters in Table I for the GTC and GYRO[25,26] in the simulation of the DIII-D discharge #101391. As shown by Table I, the GTC parameters are very close to those of GYRO with some differences within only a few percent.

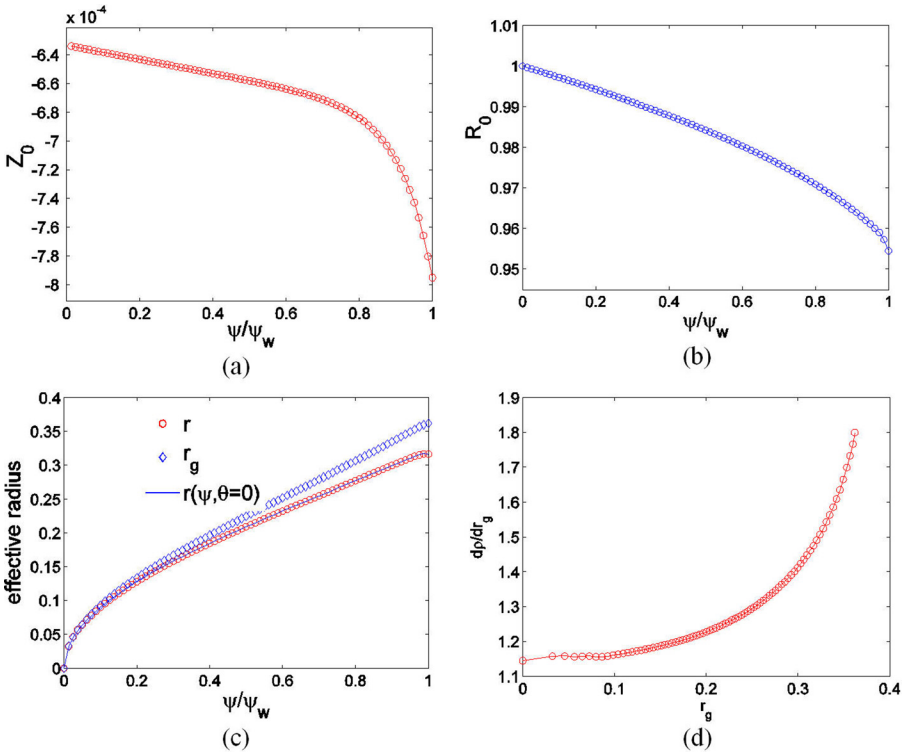

FIG. 14. Radial coordinate conventions. In the case of the DIII-D discharge #101391: (a) Z_0 in units of $R_0(0)$ varies with poloidal flux surface ψ; (b) R_0 in units of $R_0(0)$ varies with poloidal flux surface ψ; (c) effective radius r (for GTC), r_g (for GYRO) and $r(\psi, \theta = 0)$ in units of $R_0(0)$ vary with poloidal flux surface ψ; (d) $\frac{d\rho}{dr_g}$ varies with r_g in units of $R_0(0)$, which is used to calculate the effective magnetic field B_{unit}.

The definition of heat diffusivity is another issue. The GTC employs heat flux $\vec{q}$ to compute heat diffusivity χ_{gtc}

$$\vec{q} = \int d^3v \delta\vec{v}_E \delta f \left(\frac{mv^2}{2} - \frac{3}{2}T\right), \tag{D1}$$

$$\chi_{gtc} = \frac{\langle \vec{q} \cdot \nabla\psi \rangle}{n\langle |\nabla\psi|^2 \rangle \frac{\partial T}{\partial \psi}}, \tag{D2}$$

where the $\langle\rangle$ represent the flux surface average. However, the GYRO employs heat flux $\vec{Q}$ to compute heat diffusivity χ_{gyro}

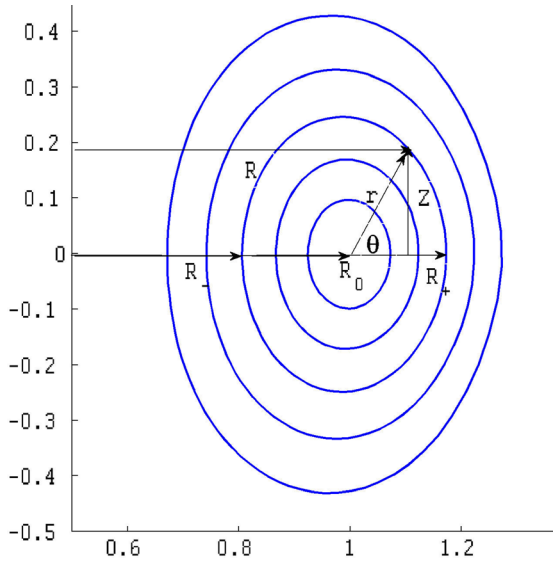

FIG. 15. Equilibrium flux surface for the DIII-D discharge # 101391. Equilibrium flux surface for the DIII-D discharge #101391 is demonstrated to show the coordinate definitions in the GTC and GYRO.

$$\vec{Q} = \int d^3v \delta\vec{v}_E \delta f \frac{mv^2}{2}, \tag{D3}$$

$$\chi_{gyro} = \frac{\langle \vec{Q} \cdot \nabla\psi \rangle}{n\langle |\nabla\psi|^2 \rangle \frac{\partial T}{\partial \psi}}. \tag{D4}$$

In principle, the symbol ψ in Eqs. (D2) and (D4) could be any flux surface function such as r_{gtc}, r_{gyro}, or ρ. Here, the symbol ψ refers specifically to the poloidal magnetic flux. The relationship between χ_{gtc} and χ_{gyro} can be described by the following equation:

$$\chi_{gyro} = \chi_{gtc} + \frac{3}{2}\frac{T\partial n/\partial\psi}{n\partial T/\partial\psi}\frac{\langle \vec{\Gamma} \cdot \nabla\psi \rangle}{\langle |\nabla\psi|^2 \rangle \partial n/\partial\psi}, \tag{D5}$$

where the particle flux is defined as

$$\vec{\Gamma} = \int d^3v \delta\vec{v}_E \delta f. \tag{D6}$$

TABLE I. Important equilibrium parameters at $r/a = 0.6$ for the DIII-D discharge #101391. The GYRO parameters are taken from Refs. 25 and 26.

	GTC	GYRO
a (m)	0.62	0.63
R_0 (m)	1.69	1.69
B_0 (T)	2.11	2.1
$\rho*$	0.0027	0.0026
q	1.55	1.59
T_e (kev)	1.28	1.25
χ_{GB} (m^2/s)	1.14	1.02

[1]E. J. Doyle, W. A. Houlberg, Y. Kamada, V. Mukhovatov, T. H. Osborne, A. Polevoi, G. Bateman, J. W. Connor, J. G. Cordey, T. Fujita, X. Garbet, T. S. Hahm, L. D. Horton, A. E. Hubbard, F. Imbeaux, F. Jenko, J. E. Kinsey, Y. Kishimoto, J. Li, T. C. Luce, Y. Martin, M. Ossipenko, V. Parail, A. Peeters, T. L. Rhodes, J. E. Rice, C. M. Roach, V. Rozhansky, F. Ryter, G. Saibene, R. Sartori, A. C. C. Sips, J. A. Snipes, M. Sugihara, E. J. Synakowski, H. Takenaga, T. Takizuka, K. Thomsen, M. R. Wade, and H. R. Wilson, ITPA Transport Physics Topical Group, ITPA Confinement Database and Modelling Topical Group and ITPA Pedestal and Edge Topical Group, "Plasma confinement and transport," Nucl. Fusion **47**(6), S18–S127 (2007).
[2]W. Horton, "Drift waves and transport," Rev. Mod. Phys. **71**(3), 735–778 (1999).
[3]J. Q. Li and Y. Kishimoto, "Gyrofluid simulation of ion-scale turbulence in tokamak plasmas," Commun. Comput. Phys. **4**(5), 1245–1257 (2008).
[4]D. W. Ross, W. M. Tang, and J. C. Adam, "Study of trapped electron instabilities driven by magnetic curvature drifts," Phys. Fluids **20**(4), 613–618 (1977).
[5]Z. Lin, T. S. Hahm, W. W. Lee, W. M. Tang, and R. B. White, "Turbulent transport reduction by zonal flows: Massively parallel simulations," Science **281**(5384), 1835–1837 (1998).
[6]A. M. Dimits, B. I. Cohen, W. M. Nevins, and D. E. Shumaker, "Parameter dependences of ion thermal transport due to toroidal ITG turbulence," Nucl. Fusion **41**(11), 1725–1732 (2001).
[7]Y. Xiao, P. J. Catto, and W. Dorland, "Effects of finite poloidal gyroradius, shaping, and collisions on the zonal flow residual," Phys. Plasmas **14**(5), 055910 (2007).
[8]Z. Lin, S. Ethier, T. S. Hahm, and W. M. Tang, "Size scaling of turbulent transport in magnetically confined plasmas," Phys. Rev. Lett. **88**(19), 195004 (2002).
[9]Y. Xiao and Z. Lin, "Convective motion in collisionless trapped electron mode turbulence," Phys. Plasmas **18**(11), 110703 (2011).
[10]C. Holland, A. E. White, G. R. McKee, M. W. Shafer, J. Candy, R. E. Waltz, L. Schmitz, and G. R. Tynan, "Implementation and application of two synthetic diagnostics for validating simulations of core tokamak turbulence," Phys. Plasmas **16**(5), 052301 (2009).
[11]T. L. Rhodes, C. Holland, S. P. Smith, A. E. White, K. H. Burrell, J. Candy, J. C. DeBoo, E. J. Doyle, J. C. Hillesheim, J. E. Kinsey, G. R. McKee, D. Mikkelsen, W. A. Peebles, C. C. Petty, R. Prater, S. Parker, Y. Chen, L. Schmitz, G. M. Staebler, R. E. Waltz, G. Wang, Z. Yan, and L. Zeng, "L-mode validation studies of gyrokinetic turbulence simulations via multiscale and multifield turbulence measurements on the DIII-D tokamak," Nucl. Fusion **51**(6), 063022 (2011).
[12]C. Holland, L. Schmitz, T. L. Rhodes, W. A. Peebles, J. C. Hillesheim, G. Wang, L. Zeng, E. J. Doyle, S. P. Smith, R. Prater, K. H. Burrell, J. Candy, R. E. Waltz, J. E. Kinsey, G. M. Staebler, J. C. DeBoo, C. C. Petty, G. R. McKee, Z. Yan, and A. E. White, "Advances in validating gyrokinetic turbulence models against L- and H-mode plasmas," Phys. Plasmas **18**(5), 056113 (2011).
[13]I. Holod, W. L. Zhang, Y. Xiao, and Z. Lin, "Electromagnetic formulation of global gyrokinetic particle simulation in toroidal geometry," Phys. Plasmas **16**(12), 122307 (2009).
[14]W. Deng, Z. Lin, I. Holod, Z. Wang, Y. Xiao, and H. Zhang, "Linear properties of reversed shear Alfven eigenmodes in the DIII-D tokamak," Nucl. Fusion **52**(4), 043006 (2012).
[15]D. A. Spong, E. M. Bass, W. Deng, W. W. Heidbrink, Z. Lin, B. Tobias, M. A. Van Zeeland, M. E. Austin, C. W. Domier, and N. C. Luhmann, Jr., "Verification and validation of linear gyrokinetic simulation of Alfven eigenmodes in the DIII-D tokamak," Phys. Plasmas **19**(8), 082511 (2012).
[16]Z. Wang, Z. Lin, I. Holod, W. W. Heidbrink, B. Tobias, M. Van Zeeland, and M. E. Austin, "Radial localization of toroidicity-induced Alfven eigenmodes," Phys. Rev. Lett. **111**(14), 145003 (2013).
[17]D. P. Fulton, Z. Lin, I. Holod, and Y. Xiao, "Microturbulence in DIII-D tokamak pedestal. I. Electrostatic instabilities," Phys. Plasmas **21**(4), 042110 (2014).
[18]J. McClenaghan, Z. Lin, I. Holod, and W. Deng, "Verification of gyrokinetic particle simulation of current-driven instability in fusion plasmas. I. Internal kink mode," Phys Plasmas **21**, 122519 (2014).
[19]J. Bao, Z. Lin, A. Kuley, and Z. X. Lu, "Particle simulation of lower hybrid wave propagation in fusion plasmas," Plasma Phys. Controlled Fusion **56**, 95020 (2014).
[20]Q. Ren, M. S. Chu, L. L. Lao, and R. Srinivasan, "High spatial resolution equilibrium reconstruction," Plasma Phys. Controlled Fusion **53**(9), 095009 (2011).
[21]L. L. Lao, J. M. Greene, T. S. Wang, F. J. Helton, and E. M. Zawadzki, "3-dimensional toroidal equilibria and stability by a variational spectral method," Phys. Fluids **28**(3), 869–877 (1985).
[22]S. P. Hirshman and J. C. Whitson, "Steepest-descent moment method for 3-dimensional magnetohydrodynamic equilibria," Phys. Fluids **26**(12), 3553–3568 (1983).
[23]R. J. Goldston, D. C. McCune, H. H. Towner, S. L. Davis, R. J. Hawryluk, and G. L. Schmidt, "New techniques for calculating heat and particle source rates due to neutral beam injection in axisymmetric tokamaks," J. Comput. Phys. **43**(1), 61–78 (1981).
[24]W. W. Lee, "Gyrokinetic particle simulation-model," J. Comput. Phys. **72**(1), 243–269 (1987).
[25]R. E. Waltz, J. Candy, and M. Fahey, "Coupled ion temperature gradient and trapped electron mode to electron temperature gradient mode gyrokinetic simulations," Phys. Plasmas **14**(5), 056116 (2007).
[26]J. Candy and R. E. Waltz, "Anomalous transport scaling in the DIII-D tokamak matched by supercomputer simulation," Phys. Rev. Lett. **91**(4), 045001 (2003).
[27]T. S. Hahm, "Nonlinear gyrokinetic equations for tokamak microturbulence," Phys. Fluids **31**(9), 2670–2673 (1988).
[28]Z. Lin, Y. Nishimura, Y. Xiao, I. Holod, W. L. Zhang, and L. Chen, "Global gyrokinetic particle simulations with kinetic electrons," Plasma Phys. Controlled Fusion **49**(12B), B163–B172 (2007).
[29]S. E. Parker and W. W. Lee, "A fully nonlinear characteristic method for gyrokinetic simulation," Phys. Fluids B **5**(1), 77–86 (1993).
[30]W. W. Lee, "Gyrokinetic approach in particle simulation," Phys. Fluids **26**(2), 556–562 (1983).
[31]J. L. V. Lewandowski, G. Rewoldt, S. Ethier, W. W. Lee, and Z. Lin, "Global particle-in-cell simulations of microturbulence with kinetic electrons," Phys. Plasmas **13**(7), 072306 (2006).
[32]Z. Lin and W. W. Lee, "Method for solving the gyrokinetic Poisson equation in general geometry," Phys. Rev. E **52**(5), 5646–5652 (1995).
[33]H. S. Zhang and Z. Lin, "Trapped electron damping of geodesic acoustic mode," Phys. Plasmas **17**(7), 072502 (2010).
[34]S. Balay, S. Abhyankar, M. F. Adams, J. Brown, P. Brune, K. Buschelman, V. Eijkhout, W. D. Gropp, D. Kaushik, M. G. Knepley, L. C. McInnes, K. Rupp, B. F. Smith, and H. Zhang, PETSc Web page, 2014; Available from: http://www.mcs.anl.gov/petsc.
[35]R. B. White and M. S. Chance, "Hamiltonian guiding center drift orbit calculation for plasmas of arbitrary cross-section," Phys. Fluids **27**(10), 2455–2467 (1984).